A Real-Time Movement Artifact Removal Method for Ambulatory Brain-Computer Interfaces

Young-Eun Lee, No-Sang Kwak, and Seong-Whan Lee, *Fellow, IEEE*

***Abstract*— Recently, practical brain-computer interfaces (BCIs) have been widely investigated for detecting human intentions in real world. However, performance differences still exist between the laboratory and the real world environments. One of the main reasons for such differences comes from the user's unstable physical states (e.g., human movements are not strictly controlled), which produce unexpected signal artifacts. Hence, to minimize the performance degradation of electroencephalography (EEG)-based BCIs, we present a novel artifact removal method named constrained independent component analysis with online learning (cIOL). The cIOL can find and reject the noise-like components related to human body movements (i.e., movement artifacts) in the EEG signals. To obtain movement information, isolated electrodes are used to block electrical signals from the brain using high-resistance materials. We estimate artifacts with movement information using constrained independent component analysis from EEG signals and then extract artifact-free signals using online learning in each sample. In addition, the cIOL is evaluated by signal processing under 16 different experimental conditions (two types of EEG devices × two BCI paradigms × four different walking speeds). The experimental results show that the cIOL has the highest accuracy in both scalp- and ear-EEG, and has the highest signal-to-noise ratio in scalp-EEG among the state-of-the-art methods, except for the case of steady-state visual evoked potential at 2.0 m/s with superposition problem.**

***Index Terms*— Electroencephalography (EEG), artifact removal, constrained independent component analysis (cICA), online learning, ambulatory environment.**

Manuscript received June 16, 2020; revised October 9, 2020; accepted November 11, 2020. Date of publication November 24, 2020; date of current version January 29, 2021. This work was supported by the Institute for Information & Communications Technology Planning & Evaluation (IITP) grant funded by the Korea Government (MSIT) (Development of BCI based Brain and Cognitive Computing Technology for Recognizing User's Intentions Using Deep Learning) under Grant 2017-0-00451, (Development of Intelligent Pattern Recognition Softwares for Ambulatory Brain Computer Interface) under Grant 2015-0-00185, and (Artificial Intelligence Graduate School Program, Korea University) under Grant 2019-0-00079. *(Corresponding author: Seong-Whan Lee.)*

Young-Eun Lee is with the Department of Brain and Cognitive Engineering, Korea University, Seoul 02841, South Korea (e-mail: ye_lee@korea.ac.kr).

No-Sang Kwak is with the Digital Tech. Center, SK Holdings C&C, Seongnam 13558, South Korea (e-mail: nskwak@sk.com).

Seong-Whan Lee is with the Department of Artificial Intelligence, Korea University, Seoul 02841, South Korea, and also with the Department of Brain and Cognitive Engineering, Korea University, Seoul 02841, South Korea (e-mail: sw.lee@korea.ac.kr).

This article has supplementary downloadable material available at https://doi.org/10.1109/TNSRE.2020.3040264, provided by the authors.

Digital Object Identifier 10.1109/TNSRE.2020.3040264

I. Introduction

BRAIN-COMPUTER interfaces (BCIs) are technical systems that help impaired people communicate with and control a computer or robot by decoding human intentions from brain signals [1]. There are several state-of-the-art BCI systems that are used to increase the performance of identification of user intentions under laboratory conditions [2], [3]. However, BCIs are difficult to use under ambulatory conditions for recognition of human intentions in the real world [4]–[7]. Under ambulatory conditions, some movement artifacts may arise from external sources, such as head movements, muscle activities, and even motions of electrodes and cables connected on the skin [8]. These artifacts distort the original electroencephalography (EEG) signals to a large extent by increasing the challenges associated with the detection of user intentions. Several studies based on BCIs under ambulatory conditions have been actively conducted by applying artifact removal methods at the preprocessing stage [9]–[14] or using advanced approaches for the feature extraction or the classification stage to better understand user intentions effectively [15]–[17].

Artifact removal methods include separation of components by their statistical characteristics and subtraction of reference signals from EEG signals. Many attempts have been made to remove artifacts based on independent component analysis (ICA) or principal component analysis (PCA). In particular, artifact subspace reconstruction (ASR) [18], [19] is a PCA-based real-time artifact removal method for short-term segments, such as a second. In each segment, ASR repeats the PCA algorithm toward distinguishing subspaces statistically from baseline data, such as under the standing condition, and then reconstructs the subspace. A modified version of ASR using Riemannian geometry was recently introduced as Riemannian ASR (rASR) [14]. Adaptive mixture ICA (AMICA) [20] is a maximum likelihood estimation of the ICA with a mixture model updated adaptively using a Newton method; it removes the most mutually dependent component among the EEG channels by calculating the equivalent dipole models fitting cortical locations. ASR and AMICA are the most widely used methods for removing movement artifacts; some studies have combined the two methods to enhance the performance [5]. Canonical correlation analysis (CCA) based on second-order statistics aims to determine sources that are maximally auto-correlated and mutually uncorrelated, and is used to compare original and time-delayed EEG data [11].

There have also been several attempts to remove artifacts using reference signals, such as signals obtained from accelerometers or isolated electrodes. Gwin *et al.* first attempted to remove movement artifacts during walking or running using gait-based template matching via AMICA [9]. However, this method has the disadvantage that the windows to apply the method are locked to the gait events. In addition, artifacts are considerably diverse to be represented by just one template [10]. Instead of locked-in-gait methods, an adaptive filter has been applied in small time segments to remove movement artifacts using reference signals obtained from accelerometers [21], [22]. By contrast, isolated electrodes were first suggested after it was found that the accelerometers could not encode movement artifacts well [23]–[25]. Isolated electrodes were used to represent movement artifacts, which block EEG signals from the scalp, using materials with high-resistance such as silicon. Nordin *et al.* recently developed dual electrodes, which are placed at the same location of isolated electrode and electrode for brain signals. They suggested a new method to remove artifacts based on fast Fourier transform (FFT) using signals obtained from isolated electrodes [13], [26].

The performance of movement artifact removal methods can be evaluated using statistical analysis, such as power spectral density (PSD) and BCI performance from the viewpoint of the accuracy and signal-to-noise ratio (SNR). Several studies have been conducted to improve BCI performance in the walking environment using artifact removal methods [7], [27]. Event-related potential (ERP) [28], [29] and steady-state visual evoked potential (SSVEP) are the most widely used BCI paradigms for evaluating signal quality during walking [4], [30].

In addition to controlling the noisy environment for practical BCIs, the development of simple hardware to measure EEG signals has attracted interest. Dry EEG and a small number of channel devices are frequently used in the real world [31]–[34]. Among these, ear-EEG has recently been investigated by several researchers to provide greater ease of use, and its feasibility was validated by analysis of the signal quality using various BCI paradigms. Several studies [35], [36] have demonstrated the feasibility of ear-EEG signals in steady-state and transient ERP paradigm experiments. Compared to scalp-EEG, the signal amplitude in ear-EEG was similar for transient responses and smaller for steady-state responses, whereas the SNR was retained for steady-state responses and lower for transient responses [35]. Moreover, around-ear-EEG, i.e., cEEGrid, has been designed, wherein only a few electrodes are placed around the ear [33]. The cEEGrid could preserve the ERP signals and had similar performance to scalp-EEG [37]. Moreover, there have been attempts to enhance the performance using signals from ear-EEG. Kwak *et al.* [38] estimated signals based on regression methods from ear-EEG signals to enhance the BCI performance of cEEGrid. Although the SSVEP was captured at the location of the occipital lobe, errors could be estimated and corrected to identify user intentions.

Thus, for practical BCIs, it is necessary to develop artifact removal techniques in the preprocessing stage and improve performance while using simple hardware. Herein, we propose a movement artifact removal method by applying constrained ICA with online learning (cIOL) using information from isolated electrodes compared with information from inertial measurement unit (IMU) sensors. Our main contributions are as follows: (1) Development of a real-time preprocessing algorithm to enhance recognition of human intentions by obtaining estimated artifacts from EEG signals. (2) Quantitative evaluation of artifact removal methods using two BCI paradigms, ERP and SSVEP, to analyze the noise reduction effect in the time and frequency domains. (3) Analysis of the effect of noise level on artifact removal methods by performing experiments at various gait speeds of 0, 0.8, 1.6, and 2.0 m/s. (4) Performing experiments using ear-EEG and comparing the results with those obtained for scalp-EEG to improve practical BCI usability.

II. Materials and Method

A. Experimental Design

1) Subjects: This experiment was conducted with 18 healthy subjects (four females, age: 24.5 ± 3.1 years). All subjects participated in ERP tasks, of which only 13 subjects executed a light running session (2.0 m/s). Among the 18 subjects, 17 participated in SSVEP tasks, of which only 13 subjects executed a light running session. None of the subjects had any history of neurological, psychiatric, or other pertinent disease that might have affected the experimental results. All subjects provided written informed consent before the experiments. All experiments were conducted in accordance with the Declaration of Helsinki. This study was reviewed and approved by the Korea University Institutional Review Board (KUIRB-2019-0194-01).

2) Data Acquisition: The subjects stood on a treadmill 80 ($\pm$5) cm in front of a 24-in LCD monitor (refresh rate: 60 Hz, resolution: $1,920 \times 1,080$) during the experiments. They stood (0 m/s), walked at 0.8 and 1.6 m/s, or lightly ran at 2.0 m/s (Fig. 1a) according to the specifications of the experiments.

We simultaneously collected data from three different devices; specifically EEG signals from the scalp, EEG signals from the ear, and signals from IMU sensors. For scalp-EEG, we used BrainAmp (Brain Product GmbH) and Ag/AgCl electrodes to acquire signals with 32 EEG channels, 5 isolated channels, and 4 channels of electrooculography (EOG) according to the 10/20 international system (Fig. 1b). Reference and ground electrodes were mounted at FCz and Fpz, and isolated scalp-EEG channels were at C1, C2, CPz, P1, and P2. The sampling rate was 500 Hz, and all impedances were maintained below 10 $k\Omega$.

For ear-EEG, we used a Smarting system (mBrainTrain LLC) and cEEGrid electrodes with 10 channels on the left side (L1–L10), 8 channels on the right side (R1–R8), and ground and reference electrodes on the middle of the right side. We acquired 14 channels of ear-EEG and 4 channels of isolated ear-EEG located at L3, L8, R3, and R6. The sampling rate was 500 Hz, and all impedances were maintained below 10 $k\Omega$.

We used three wearable IMU sensors (APDM wearable technologies) to record movement on the head, left ankle, and

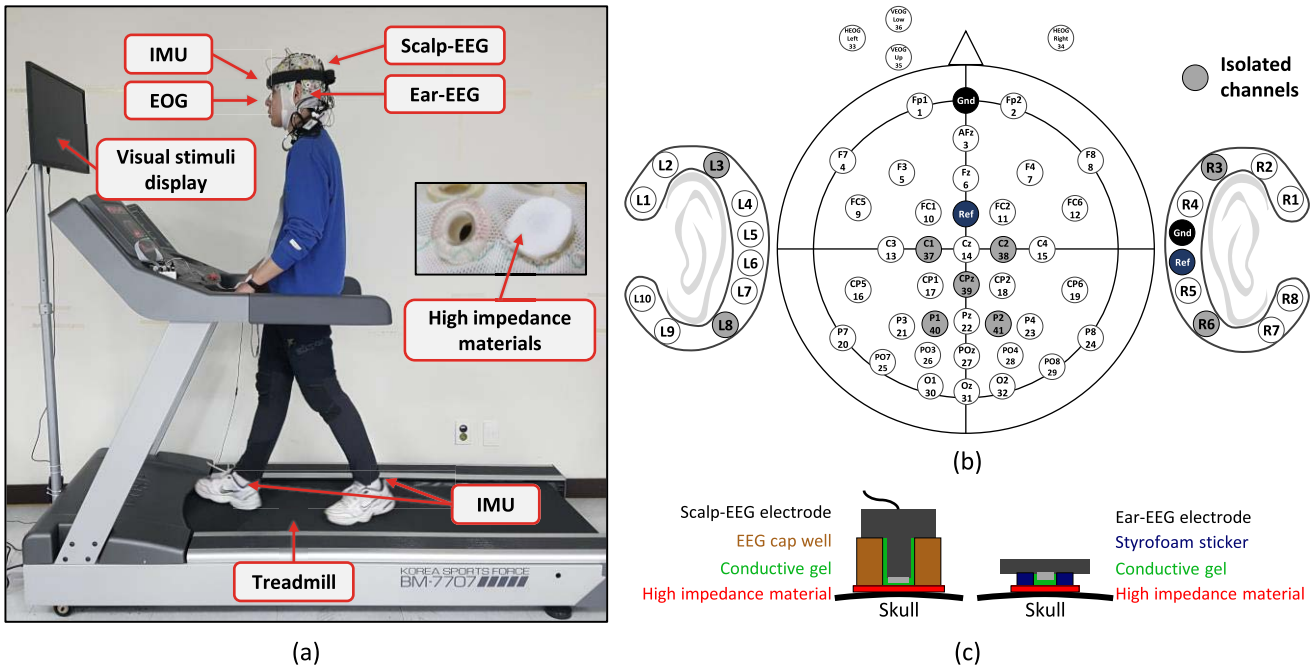

Fig. 1. Design of the experiment. (a) Experimental setup and recorders. Subjects stood (0 m/s), walked (0.8 and 1.6 m/s), and ran (2.0 m/s) on a treadmill. They watched a display presenting stimuli of BCI paradigms. Signals from scalp-EEG, ear-EEG around both ears, EOGs placed above and below the left eye to measure the vertical EOGs (VEOGs) and on left and right temples to measure the horizontal EOGs (HEOGs), and IMU sensors comprising nine channels, including three-axis accelerometers, three-axis gyroscopes, and three-axis magnetometers, placed on the forehead, and left and right ankles were recorded during the experiments. Reference signals of movement artifacts were recorded from isolated channels that were blocked using high-impedance materials. (b) Channel placement of the used modalities including scalp-EEG, ear-EEG, EOG, and isolated electrodes colored with gray. (c) Conceptual schematic of isolated channel adding high impedance materials to normal electrodes for scalp- and ear-EEG.

right ankle. The IMU sensors comprise 9 channels including three-axis accelerometers, three-axis gyroscopes, and three-axis magnetometers at a sampling rate of 128 Hz.

Among the scalp- and ear-EEG, we blocked several channels to make isolated channels using high-impedance materials, such as coated fabric, to acquire only artifact signals and not EEG signals (Fig. 1c). We used a multimeter to measure the resistances of the isolated electrodes from the ground and set them to 1.9 ± 0.4 $M\Omega$ [23]. The isolated channel location was chosen based on sites with prominent movement artifacts on the scalp [23], avoiding Cz with important information for the BCI paradigms. In the case of ear-EEG, a comprehensive location was selected by spreading isolated channels.

3) Experimental Paradigm: We conducted experiments using two BCI paradigms: ERP and SSVEP. ERP is an electrical potential induced in the central and parietal cortex in response to a cognitive task [32]. Attention to the target induces P300 components, which have task-relevant peaks at 300 ms after the target stimulus. In this experiment, the paradigm was executed with target ('OOO') and non-target ('XXX') characters. The ratio of the target was 0.2, and the total number of trials was 300. In a trial, a stimulus was presented for 0.5 s, and a cross was shown to indicate a random rest for 0.5–1.5 s (Fig. 2a).

SSVEP was evoked in the occipital cortex when the user concentrated on repetitive visual stimuli; the frequency domain of the EEG signals increased in amplitude at the same frequency as the visual stimulus. White-colored SSVEP stimuli were designed to flicker at 5.45, 8.57, and 12 Hz on a 60-Hz LCD monitor [39]. Each stimulus was shown for 4 s with an inter-stimulus interval of 4 s (Fig. 2b).

B. Processing

The process of artifact removal is shown in Fig. 3. The collected EEG signals and reference signals such as isolated channels and IMU signals were the system input, whereas the artifact-free EEG signals were the output. All signals were pre-operated to remove EOG-related channels and bad channels, down sample, and filter in a certain frequency band. A constrained ICA (cICA) obtained the estimated artifacts from the EEG signals using the reference signals. Recursive least squares (RLS), an algorithm for the online learning, extracted the artifact-free EEG signals with estimated artifacts. All EEG data were segmented into 2 s for real-time processing when applying the artifact removal methods. All BCI experiments and analysis were developed based on the OpenBMI (http://openbmi.org) [40], BBCI (https://github.com/bbci/bbci_public) [41], BCILAB (https://github.com/sccn/BCILAB) [42], and Psychophysics (http: //psychtoolbox.org) toolboxes [43] in MATLAB (The Mathworks, Natick, MA).

1) Pre-Operation: We removed the EOG-related channels, such as Fp1 and Fp2, and bad channels carrying abnormal signals. Bad channels were automatically removed using *flt_clean_channels* function in the BCILAB library in MATLAB with the minimum correlation of 0.4, and protected channels of Cz, Pz, POz, O1, Oz, and O2 for scalp-EEG and L10 and R8 for ear-EEG. On average, 2.3 ± 1.9 channels were

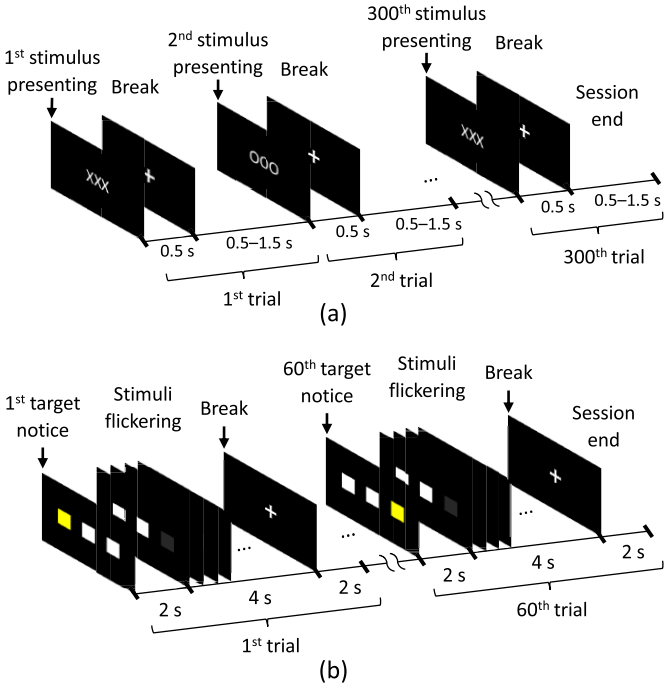

Fig. 2. Paradigms of the experiments. (a) The ERP paradigm consisting of 300 trials in a session, which presents target 'OOO' or non-target 'XXX' for 0.5 s, and takes a random break for 0.5–1.5 s. Target and non-target appear in random order, with the target ratio of 0.2. (b) SSVEP paradigm consisting of 60 trials in a session, which flickers stimuli at specific frequency of 5.45, 8.57, and 12 Hz for 4 s. Three stimuli appear in the same proportion as random order.

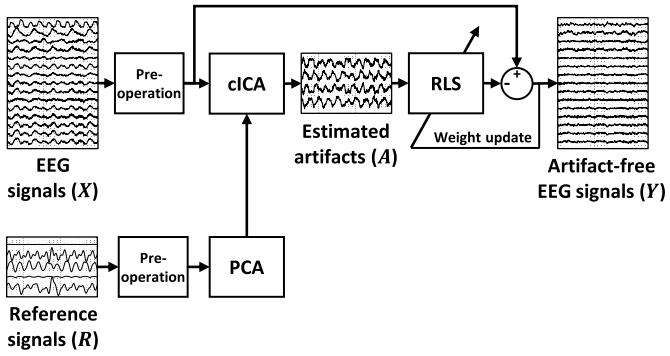

Fig. 3. Flowchart of proposed artifact removal method, cIOL. EEG signals and reference signals are inputs of cIOL, and output is artifact-free EEG signals. The cICA estimates artifacts from the EEG signals with the reference signals, and then online learning, RLS, removes artifacts, and extracts artifact-free EEG signals by updating weights for each sample.

removed, usually because of their weak adhesion to the ear-EEG and close proximity to the reference electrode. All the recorded signals were high-pass filtered at 0.5 Hz using a finite impulse response filter with a zero-phase 30^{th} order Hamming window and down sampled at 100 Hz. When we analyzed the SSVEP data, we selected the channels on the occipital visual area, including PO7, PO3, POz, PO4, PO8, O1, Oz, and O2.

2) Reference Signals: To collect the reference signals of movement artifacts, the signals of the five isolated channels were recorded, which were blocked using high-impedance materials to acquire only movement artifact signals, except brain signals [23]. The number of reference signals must be reduced to process multi-channel signals in real-time, so that PCA was performed on isolated channels. The first two components of the principle components, which contain 90% of the information of the original signals [44] were used as the reference signals and named as isolated PC in Fig. 4. Thus, four signals, i.e., the first two components and their inversion, were used as the input of the cICA.

3) cIOL: The proposed method, cICA and online learning (cIOL), can obtain artifact-free EEG signals from raw EEG signals, by inputting reference signals. The cICA handles the constrained optimization problem using Lagrange multiplier methods for the ICA problem [45], [46]. Meanwhile, online learning updates the parameters for each step to enable real-time use [47].

ICA is the blind source separation method, that can separate multivariate signals into a sum of independent components. ICA aims to find a linear demixing matrix $\mathbf{W}_{ICA}$:

$$\mathbf{A} = \mathbf{W}_{ICA}\mathbf{X} \tag{1}$$

where $\mathbf{A} = [\mathbf{a}_1, \cdots, \mathbf{a}_m]^\intercal$ denotes the blind source, $|\cdot|^\intercal$ denotes the transpose of a vector or matrix, $\mathbf{a}_i \in \mathbb{R}^{1\times T}$ denotes a single-channel blind source signal with T sample points, $\mathbf{W}_{ICA}$ denotes a linear $m \times n$ demixing matrix from the observed brain signals $\mathbf{X}$ to output $\mathbf{A}$, and $\mathbf{X} \in \mathbb{R}^{n\times T}$ denotes the n-channel observed brain signals with T sample points.

To find the optimal demixing matrix $\mathbf{W}_{ICA}$, the non-Gaussianity of the output is maximized with kurtosis or negentropy. The negentropy approach is more flexible and reliable for solving the ICA optimization problem. The cICA uses the Lagrange multiplier method to obtain a desired source from the observed brain signals by constraining them with reference signals. This constrained optimization problem using negentropy can be represented as follows:

$$\begin{aligned} &\mathbf{J}(\mathbf{W}_{cICA}) = \sum_{i=1}^{m} \alpha_i [E\{f(\mathbf{a}_i)\} - E\{f(\nu_i)\}]^2 \\ &subject\ to: \ \mathbf{g}(\mathbf{W}_{cICA}) \le 0, \quad \mathbf{h}(\mathbf{W}_{cICA}) = 0 \end{aligned} \tag{2}$$

where α_i is a constant, E is an expectation function, f is a non-quadratic function, and $\nu = [\nu_1, \cdots, \nu_m]^\intercal$ denotes the Gaussian signals, where ν_i is the same mean and variance of $\mathbf{a}_i$. $\mathbf{g}(\mathbf{W}_{cICA}) = [g_1(\mathbf{W}_{cICA}), \cdots, g_m(\mathbf{W}_{cICA})]^\intercal$ is a set of m inequality constraint functions and $\mathbf{h}(\mathbf{W}_{ICA}) = [h_1(\mathbf{W}_{cICA}), \cdots, h_m(\mathbf{W}_{cICA})]^\intercal$ is a set of m equality constraint functions. We specified the function f as a log-cosh function, defined as $f(x) = log(cosh(x))$. The constraint function can be defined as:

$$g_i(\mathbf{W}_{cICA}) = \varepsilon(\mathbf{a}_i, \mathbf{r}_i) - \xi \tag{3}$$

$$h_i(\mathbf{W}_{cICA}) = E(\mathbf{a}_i^2) - 1 \tag{4}$$

where $\varepsilon(\cdot)$ is the closeness measurement obtained by calculating the square of the distance between two variables, $\mathbf{r}_i$ denotes the i-th reference signals referring to isolated signals, and ξ is a small threshold.

Based on the aforementioned formula, the Lagrangian function $\mathcal{L}$ for the problem can be written as:

$$\begin{aligned}\mathcal{L}(\mathbf{W}_{cICA}, \mu, \lambda) = &\mathbf{J}(\mathbf{W}_{cICA}) \\ &+ \mu \max\{0, \mathbf{g}(\mathbf{W}_{cICA})\} + \frac{1}{2}\gamma \left\|\mathbf{g}(\mathbf{W}_{cICA})\right\|^2 \\ &+ \lambda \mathbf{h}(\mathbf{W}_{cICA}) + \frac{1}{2}\gamma \left\|\mathbf{h}(\mathbf{W}_{cICA})\right\|^2 \end{aligned} \tag{5}$$

where $\mu = [\mu_1, \cdots, \mu_m]^\intercal$ and $\lambda = [\lambda_1, \cdots, \lambda_m]^\intercal$ are two sets of Lagrangian multipliers, γ is the scalar penalty parameter, and $\|\cdot\|$ denotes the Euclidean norm for the weight decay with L_2-norm. To optimize the problem, using a Newton-like gradient method, the first- and second-order Lagrangian were used to update $\mathbf{W}_{cICA}$ as:

$$\begin{aligned}\mathbf{W}_{cICA}(k+1) = &\mathbf{W}_{cICA}(k) \\ &- \eta \left(\nabla^2_{\mathbf{W}_{cICA}} \mathcal{L}\right)^{-1} \nabla_{\mathbf{W}_{cICA}} \mathcal{L} \end{aligned} \tag{6}$$

where k denotes the iterative index and η denotes the learning rate and $\left(\nabla^2_{\mathbf{W}_{cICA}} \mathcal{L}\right)^{-1}$ is the inverse matrix of the second-order Lagrangian. The Lagrangian multipliers μ and λ can be iteratively updated as follows:

$$\mu(k+1) = \max\{0, \mu(k) + \gamma\, \mathbf{g}(k)\} \tag{7}$$

$$\lambda(k+1) = \lambda(k) + \gamma\, \mathbf{h}(k) \tag{8}$$

Online learning is a sample-by-sample filter that adapts the weights and finds the optimal weights to transform reference signals to primary signals [47], [48]. We used the RLS algorithm for online learning approaching an adaptive filter that recursively finds the coefficients minimizing a weighted linear least squares cost function. The RLS formula is given by:

$$\mathbf{y}_i = \mathbf{x}_i - \mathbf{V}_i^\intercal \mathbf{a}_i \tag{9}$$

where, $\mathbf{x}_i$ is contained in $\mathbf{X} = [\mathbf{x}_1, \cdots, \mathbf{x}_t]$, a set of t samples of the observed brain signals having filter order t, $\mathbf{x}_i \in \mathbb{R}^{n\times 1}$ denotes the n-channel signals with a single sample point, $\mathbf{a}_i$ is contained in $\mathbf{A} = [\mathbf{a}_1, \cdots, \mathbf{a}_t]$, a set of t samples of estimated artifacts from cICA, $\mathbf{a}_i \in \mathbb{R}^{m\times 1}$ denotes the m-source signals with a single sample point, and $\mathbf{V}_i$ is the i-th iteration of an $m \times n$ mixing matrix. The weight matrix of the RLS for $\mathbf{V}$ is updated recursively as follows:

$$\mathbf{V}_i = \mathbf{V}_{i-1} + \mathbf{C}\mathbf{e} \tag{10}$$

$$\mathbf{e} = \mathbf{x}_i - \mathbf{V}_{i-1}^\intercal \mathbf{a}_i \tag{11}$$

where $\mathbf{C}$ is the gain vector and $\mathbf{e}$ is the error of the RLS. The gain vector is obtained by a recursive algorithm, which is denoted by:

$$\mathbf{C} = \mathbf{P}_{i-1}\mathbf{a}_i \left(\beta + \mathbf{a}_i^\intercal \mathbf{P}_{i-1}\mathbf{a}_i\right)^{-1} \tag{12}$$

$$\mathbf{P}_i = \beta^{-1}\left(\mathbf{P}_{i-1} - \mathbf{C}\mathbf{a}_i^\intercal \mathbf{P}_{i-1}\right) \tag{13}$$

where $\mathbf{P}$ is the inverse matrix of the Woodbury matrix identity, which is the sample covariance matrix for $\mathbf{a}$, and β is a forgetting factor that corresponds to the contribution of previous samples to the covariance matrix.

In this study, the inputs of cICA were EEG signals and reference signals from IMU or isolated electrode. The cICA used reference signals to extract the estimated artifacts, originating from the EEG signals. Meanwhile, the inputs of RLS, an online learning algorithm, were raw EEG signals and estimated artifacts from cICA, and the output was cleaned EEG signals. For real-time performance, all algorithms were segmented and operated with a 2-s window.

4) Classification: For the ERP paradigm, features were extracted by averaging the potential values over time at specific intervals, every 50 ms between 200 ms and 450 ms, for each channel [49]. The classification was performed using linear discriminant analysis (LDA). The LDA optimizes the projection vector $\mathbf{W}_{LDA}$, and maximizing $\mathbf{Q}$ as follows:

$$\max_{\mathbf{W}_{LDA}} \mathbf{Q} = \frac{\mathbf{W}_{LDA}^\intercal \mathbf{S}_b \mathbf{W}_{LDA}}{\mathbf{W}_{LDA}^\intercal \mathbf{S}_w \mathbf{W}_{LDA}} \tag{14}$$

where $\mathbf{S}_b$ refers to the covariance matrix between the classes and $\mathbf{S}_w$ refers to the covariance matrix within the classes.

For the SSVEP paradigm, classification was performed using CCA. The CCA-based classifier is a multivariate statistical method that maximizes the correlation between two signals, without a training phase. The CCA-based classifier determines the weight matrices, $\mathbf{W}_{CCA_b}$, and $\mathbf{W}_{CCA_z}$, as follows:

$$\begin{aligned}&\max_{\mathbf{W}_{CCA_b}, \mathbf{W}_{CCA_z}} \rho(\mathbf{b}, \mathbf{z}) \\ &= \frac{E[\mathbf{W}_{CCA_b}^\intercal \mathbf{b}\mathbf{z}^\intercal \mathbf{W}_{CCA_z}]}{\sqrt{E[\mathbf{W}_{CCA_b}^\intercal \mathbf{b}\mathbf{b}^\intercal \mathbf{W}_{CCA_b}] E[\mathbf{W}_{CCA_z}^\intercal \mathbf{z}\mathbf{z}^\intercal \mathbf{W}_{CCA_z}]}} \end{aligned} \tag{15}$$

where $\mathbf{b}$ refers to the observed EEG signals and $\mathbf{z}$ refers to a set of basis signals based on the presented frequency stimuli. The basis signals of the i-th stimulus were generated as follows:

$$\mathbf{z}_i = \begin{bmatrix} sin(2\pi f_i \mathbf{t}) \\ cos(2\pi f_i \mathbf{t}) \\ sin(2\pi (2f_i) \mathbf{t}) \\ cos(2\pi (2f_i) \mathbf{t}) \end{bmatrix}, \quad \mathbf{t} = \frac{1}{f_s}, \frac{2}{f_s}, \cdots, \frac{T}{f_s} \tag{16}$$

where f_i denotes the i-th stimulus with 5.45, 8.57, and 12 Hz, T is the number of sampling points, and f_s denotes the sampling frequency.

C. Evaluation

To evaluate the proposed artifact removal method, we compared our proposed method, cIOL, with the state-of-the-art artifact removal methods, which include ASR [18], rASR [14], and FFT-based method [13]. In cases where reference signals were required, such as FFT-based method, isolated PC signals were used for fair comparison. We evaluated the results via statistical analysis to measure the signal properties using the PSD, whereas BCI performance was implemented using the area under the receiver operating characteristic (ROC) curve (AUC) for the ERP, accuracy for the SSVEP, and the approximated SNR for both paradigms. Since the actual signals always contain noise signals, the SNR is approximated with the ratio of signals + noise to noise [50], [51].

The AUC of the ERP, displays the true positive rate over the false positive rate of the results. As the numbers of the target and non-target differed, we used the AUC to

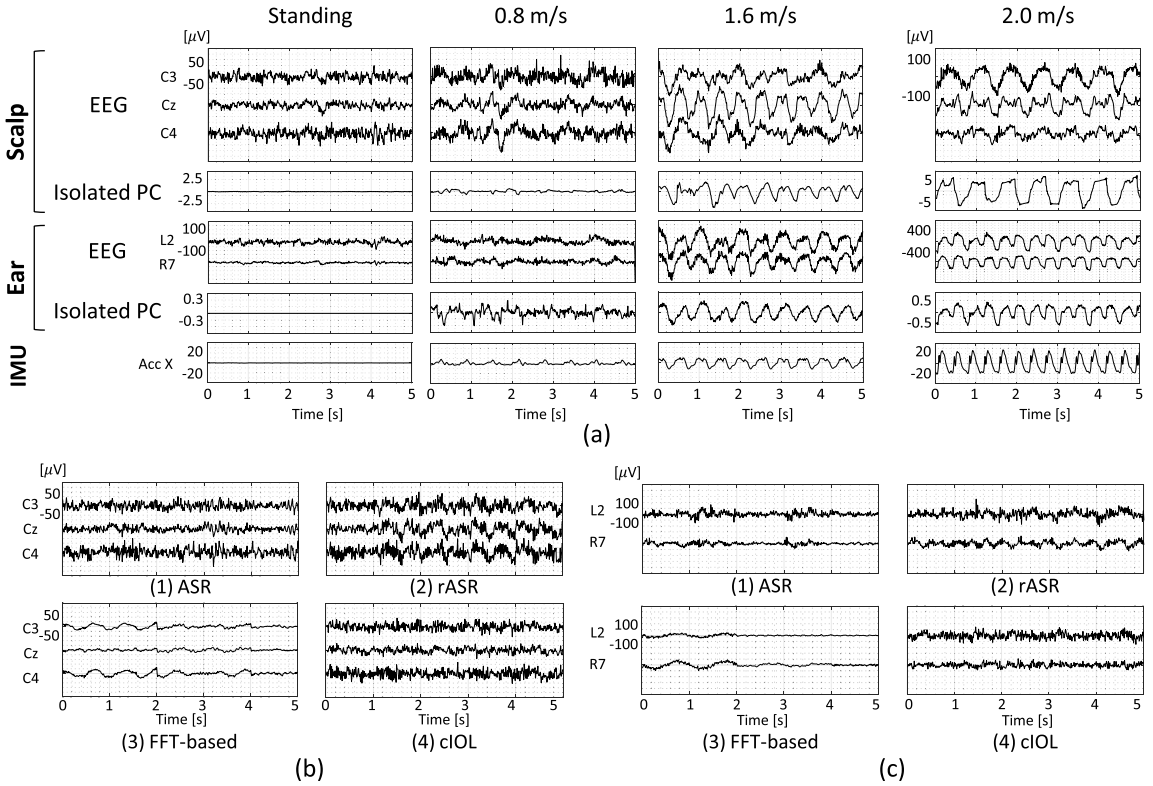

Fig. 4. Examples of raw signals for all modalities at each speed and EEG signals after applying each artifact removal method. (a) Plots showing examples of the raw signals for 5 s in scalp-EEG, scalp isolated PC, ear-EEG, ear isolated PC, and IMU signals at 0, 0.8, 1.6, and 2.0 m/s. Plots showing examples of (b) scalp-EEG signals and (c) ear-EEG signals for 5 s after applying four artifact removal methods, ASR, rASR, FFT-based method, and cIOL at 1.6 m/s.

evaluate the performance, rather than the normal accuracy. The accuracy of the SSVEP was calculated as the percentage of the number of correct trials by the total number of trials.

The SNR of the ERP was approximately calculated by the root mean square (RMS) of the amplitude of P300 divided by the RMS of the average amplitude of the pre-stimulus baseline (-200–0 ms) at channel Pz [50], [52]. And the SNR of the SSVEP was approximately calculated using the ratio of the power of the target frequencies to the power of the neighboring frequencies (resolution: 0.25 Hz, number of neighbors: 12) [51].

To verify the comparison of performances among the different methods, we conducted a statistical analysis through a two-tailed paired t-test, as indicated by the asterisks shown at confidence levels of 95% and 99%.

III. Results

Fig. 4a shows five-second time series of continuous raw signals of scalp-EEG, scalp isolated PC, ear-EEG, ear isolated PC, and IMU at different speeds of 0, 0.8, 1.6, and 2.0 m/s. As the speed increased, the amplitudes of all modalities increased significantly, which would also contain noise signals on the account of walking. Both the IMU and isolated PC signals contained specific frequency components related to gait frequency. Fig. 4b and Fig. 4c respectively show five-second time series for the scalp-EEG signals and ear-EEG signals, respectively, during walking at 1.6 m/s, after applying the state-of-the-art artifact removal methods and cIOL. The performance of each method is described in the supplementary documentation.

A. ERP Performance

The ERP performance was analyzed through quantitative evaluation of ERP waves and signed r^2 values, and qualitative evaluation of AUC and SNR. Fig. 5 shows the grand averages of the ERP waves and signed r^2 values in the ERP waves after applying each artifact removal method. The P300 amplitudes of grand averages of raw signals in scalp-EEG were higher than the amplitudes of the application of the methods at every speeds, and the P300 amplitudes of cIOL in scalp-EEG were the second highest after rASR with 0.738 at 0.8 m/s, and the highest among the methods, 0.804 and 0.953 at 1.6 and 2.0 m/s, respectively. The values of P300 amplitude of the other signals in scalp-EEG were 0.882, 0.543, 0.784, and 0.197 at 0.8 m/s, 1.040, 0.369, 0.518, and 0.226 at 1.6 m/s, and 1.417, 0.345, 0.375, and 0.502 at 2.0 m/s for raw, ASR, rASR and FFT-based method, respectively. The P300 amplitudes of grand averages of raw signals in ear-EEG at 0.8 and 1.6 m/s were higher than that of the application of the methods, and the P300 amplitudes of cIOL in ear-EEG were the highest among the methods with 0.642 and 0.721 at 0.8 and 1.6 m/s, respectively. At 2.0 m/s, the P300 amplitude of cIOL, 4.172, was the highest among all signals including the raw signals. The P300 amplitudes of other signals in ear-EEG were 0.924, 0.554, 0.478, and 0.200 at 0.8 m/s, 0.973, 0.506, 0.588, and 0.198 at 1.6 m/s, and 3.631, 0.506, 0.617, and 2.134 at 2.0 m/s, for raw, ASR, rASR, and FFT-based method, respectively.

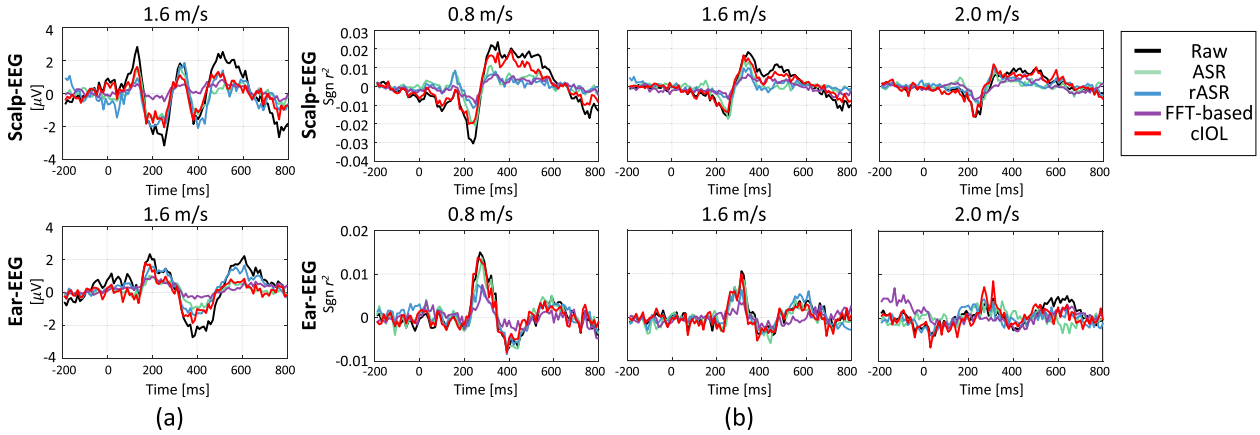

Fig. 5. Grand averages of the ERP waves and signed r^2 values. Colored line plots indicate the raw EEG signals and the signals after applying ASR, rASR, FFT-based method, and cIOL. (a) Grand averages of the ERP waves from scalp- and ear-EEG for 1 s during walking at 1.6 m/s. (b) Grand averages of signed r^2 for the ERP waves from scalp- and ear-EEG for 1 s at gait speeds of 0.8, 1.6, and 2.0 m/s.

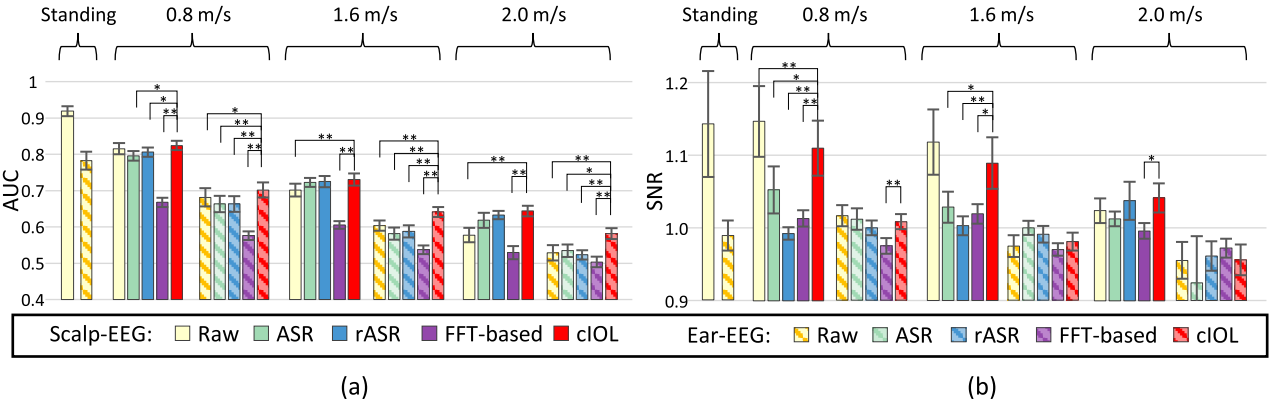

Fig. 6. ERP performances of all methods in scalp- and ear-EEG at different speeds of 0, 0.8, 1.6, and 2.0 m/s. The box plots indicate the grand averages and the standard errors across all subjects. (a) AUC and (b) SNR of the ERP shown using different colors for the different applied methods. One asterisk and two asterisks indicate significance levels of 5% and 1%,respectively, between cIOL and the corresponding method.

The absolute magnitudes of the r^2 values between 200 ms and 400 ms in both scalp- and ear-EEG for the grand average of raw signals were higher than the magnitudes of the application of the methods at every speeds, and the magnitudes of cIOL were the highest among the methods at every speeds, with 0.0140, 0.0121, and 0.0112 in scalp-EEG and 0.0070, 0.0054, and 0.0046 in ear-EEG at 0.8, 1.6, and 2.0 m/s, respectively. The absolute magnitudes of r^2 values of the other signals in scalp-EEG were 0.0192, 0.0089, 0.0052, and 0.0045 at 0.8 m/s, 0.0159, 0.0085, 0.0049, and 0.0042 at 1.6 m/s, and 0.0139, 0.0076, 0.0051, and 0.0038 at 2.0 m/s for raw, ASR, rASR, and FFT-based method, respectively. The absolute magnitudes of r^2 values of the other signals in ear-EEG were 0.0081, 0.0062, 0.0044, and 0.0025 at 0.8 m/s, 0.0059, 0.0049, 0.0036, and 0.0019 at 1.6 m/s, and 0.0047, 0.0039, 0.0030, and 0.0015 at 2.0 m/s for raw, ASR, rASR, and FFT-based method, respectively.

For the qualitative evaluation, Fig. 6a shows the AUC of the ERP in scalp- and ear-EEG during standing and movement at different speeds without and with the application of the artifact removal methods. The faster the movement speed, the lower the AUC observed in both scalp- and ear-EEG because of the signal distortion. As applying cIOL, compared to the raw signals, in scalp-EEG, the AUC increased by 0.009 ± 0.005 ($p \geq 0.05$; not significant), 0.029 ± 0.007 ($p < 0.01$), and 0.066 ± 0.017 ($p < 0.01$) at 0.8, 1.6, and 2.0 m/s, respectively. As applying cIOL in ear-EEG, the AUC increased by 0.020 ± 0.007 ($p < 0.05$), 0.037 ± 0.008 ($p < 0.01$), and 0.053 ± 0.009 ($p < 0.01$) at speeds of 0.8, 1.6, and 2.0 m/s, respectively. The cIOL in scalp- and ear-EEG had the highest AUC among the methods at all speeds.

Fig. 6b shows the SNR of the ERP in scalp- and ear-EEG during standing and movement at different speeds without and with the application of the artifact removal methods. The SNRs of the raw signals, compared to standing, in both scalp- and ear-EEG were slightly increased at 0.8 m/s and decreased at 1.6 and 2.0 m/s. After applying cIOL, compared to the raw signals, the SNR in scalp-EEG decreased by 0.037 ± 0.012 ($p < 0.01$) at 0.8 and 0.029 ± 0.015 ($p \geq 0.05$; not significant) at 1.6 m/s, but increased by 0.018 ± 0.013 ($p \geq 0.05$; not significant) at 2.0 m/s. The SNR in ear-EEG decreased by 0.008 ± 0.006 ($p \geq 0.05$; not significant) at 0.8 m/s but slightly increased by 0.006 ± 0.005 ($p \geq 0.05$; not significant) at 1.6 and 0.001 ± 0.009 ($p \geq 0.05$; not significant) at 2.0 m/s.

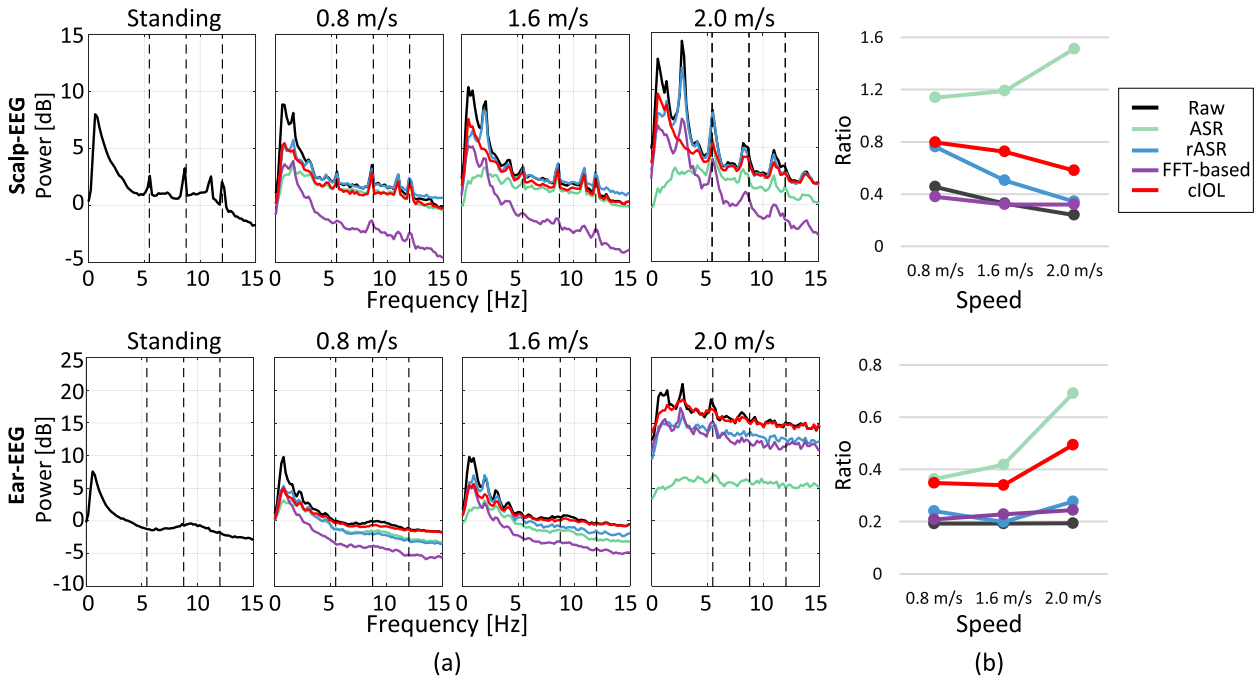

Fig. 7. Grand averages of the PSDs and the ratio of amplitudes. Colored line plots indicate the raw EEG signals and the signals after applying ASR, rASR, FFT-based method, and cIOL. (a) Grand averages of the PSDs in scalp- and ear-EEG at different speeds of 0, 0.8, 1.6, and 2.0 m/s. The dotted lines indicate the target frequencies of the SSVEP, including 5.45, 6.75, and 12 Hz. (b) Ratios of the amplitude at the target frequency to the amplitude at the stepping frequency for each method at gait speeds of 0.8, 1.6, and 2.0 m/s.

The cIOL in scalp-EEG had the highest among the methods at all speeds. Meanwhile, the SNR in ear-EEG had very low in every method, so the cIOL was significantly different only from the FFT-based method at 0.8 m/s.

B. SSVEP Performance

The SSVEP performance was analyzed through quantitative evaluation of PSD and ratio of amplitude at the target frequencies to the amplitude at stepping frequency, and qualitative evaluation of accuracy and SNR. Fig. 7a shows the grand averages of the PSD, indicating the amount of gait-related spectral components and the target frequency components of the SSVEP under the different speed conditions of 0, 0.8, 1.6, and 2.0 m/s. The averages of the stepping frequencies across all subjects were 0.76, 0.97, and 1.37 Hz at 0.8, 1.6, and 2.0 m/s, respectively. The cIOL in scalp-EEG almost removed the peaks at the stepping frequencies and maintained the amplitudes at the target frequencies at 0.8 and 1.6 m/s. At 2.0 m/s the cIOL removed well the peak at the stepping frequency, whereas did not maintain the amplitudes at the target frequencies. The reason was the superposition between the target frequency and the stepping frequency, which is described in detail in the Discussion section.

Fig. 7b shows the averages ratio of the amplitude at the target frequencies to the amplitude at stepping frequency and its harmonics. In comparison with the raw signals, the cIOL showed 1.75, 2.22, and 2.44 times higher ratio in scalp-EEG and 1.81, 1.76, and 2.55 times higher ratio in ear-EEG. Further, the cIOL had the second highest amplitude ratio after ASR. In comparison with the state-of-the-art methods, ASR, rASR, and FFT-based method, the cIOL in scalp-EEG respectively had 0.70, 1.05, and 2.10 times ratio at 0.8 m/s, 0.61, 1.44, and 2.26 times ratio at 1.6 m/s, and 0.38, 1.70, and 1.82 times ratio at 2.0 m/s. In ear-EEG, the cIOL, compared with ASR, rASR, and FFT-based method, showed 0.96, 1.45, 1.67 times ratio at 0.8 m/s, respectively, 0.81, 1.71, 1.48 times ratio at 1.6 m/s, respectively, and 0.72, 1.79, 2.03 times ratio at 2.0 m/s, respectively.

Fig. 8a shows the accuracy of the SSVEP in scalp- and ear-EEG at different speeds without and with the application of the artifact removal methods. In both scalp- and ear-EEG without the application of artifact removal methods, the higher the movement speed, the worse the performance of the SSVEP. Compared to the raw signals, after applying cIOL, the increases in the accuracy in scalp-EEG were $2.53 \pm 0.94\%$ ($p < 0.05$), $0.59 \pm 0.62\%$ ($p \geq 0.05$; not significant), and $7.55 \pm 2.84\%$ ($p < 0.05$) at 0.8, 1.6, and 2.0 m/s, respectively, whereas that in ear-EEG were $2.49 \pm 0.93\%$ ($p < 0.05$), $4.02 \pm 1.19\%$ ($p < 0.01$), and $1.39 \pm 0.90\%$ ($p \geq 0.05$; not significant), respectively. The cIOL in scalp-EEG had the highest accuracy among the methods at every speeds. The cIOL in ear-EEG had the highest accuracy among the methods at 0.8 and 1.6 m/s, whereas the accuracy of cIOL at 2.0 m/s had no significant difference, except for rASR.

Fig. 8b shows the SNR of the SSVEP in scalp- and ear-EEG at different speeds without and with the application of the artifact removal methods. The higher the movement speed, the lower the SNRs of the raw signals in scalp-EEG. Likewise, in ear-EEG, the higher the speed, excluding at 2.0 m/s, the lower the SNRs of the raw signals. After applying cIOL compared to the raw signals, the SNR in scalp-EEG slightly decreased by 0.044 ± 0.017 ($p < 0.05$) at 0.8 m/s and 0.065 ± 0.025 ($p < 0.05$) at 1.6 m/s, and considerably decreased by 0.291 ± 0.072 ($p < 0.01$) at 2.0 m/s. In ear EEG,

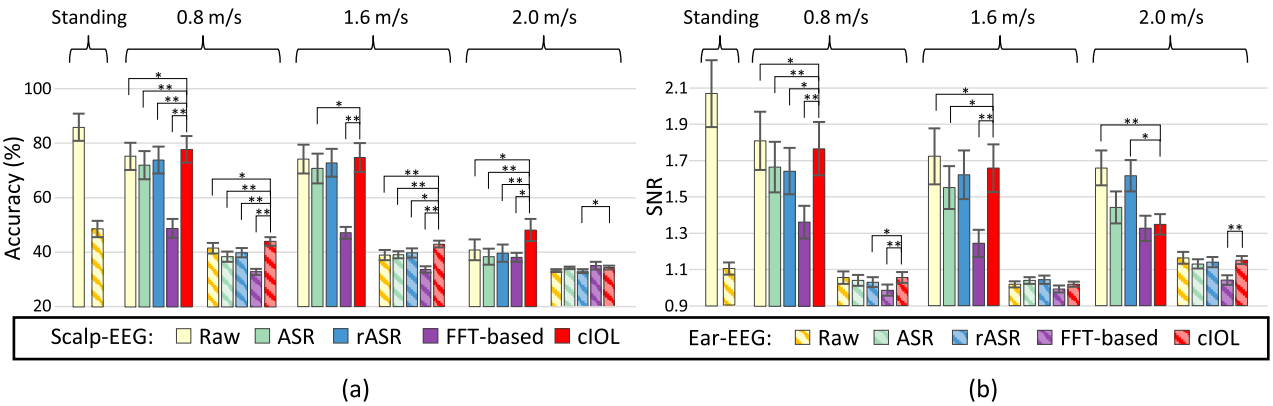

Fig. 8. SSVEP performances of all methods in scalp- and ear-EEG at different speeds of 0, 0.8, 1.6, and 2.0 m/s. The box plots indicate the grand averages and the standard errors across all subjects. (a) Accuracy and (b) SNR of the SSVEP shown with different colors for the different applied methods. One asterisk and two asterisks indicate significance levels of 5% and 1%, respectively, between cIOL and the corresponding method.

the SNR slightly increased by 0.000 ± 0.006 ($p \geq 0.05$; not significant) at 0.8 m/s and 0.001 ± 0.008 ($p \geq 0.05$; not significant) at 1.6 m/s and decreased by 0.021 ± 0.022 ($p \geq 0.05$; not significant) at 2.0 m/s. In comparison with other methods, the cIOL in scalp-EEG had the significant highest SNR among the methods at 0.8 and 1.6 m/s, whereas the cIOL at 2.0 m/s had the second lowest SNR after the FFT-based method. This was because of the superposition of target and stepping frequency, described in detail in the Discussion section. The cIOL in ear-EEG showed the highest SNR of all methods at 0.8 m/s, whereas there was no significant differences from the other methods at 1.6 and 2.0 m/s, except for the FFT-based method at 2.0 m/s.

IV. Discussion

We evaluated the cIOL in the preprocessing phase using two BCI paradigms, ERP and SSVEP, from the viewpoint of the accuracy and SNR. The cIOL estimated movement artifacts from the EEG signals, similar to the isolated electrodes using cICA, and then removed the movement artifacts by updating the weights using online learning with the estimated artifacts (Fig. 3). We compared cIOL with the state-of-the-art artifact removal methods, ASR, rASR, and FFT-based method. As the speeds increased, the extent of the accuracy increment for all paradigms became greater when cIOL was applied.

A. ERP Performance

The ERP performance indicated how the artifact removal methods affected the time-dependent features of EEG signals. In Fig. 5a, the ASR and rASR exhibited a similar shape of the ERP waves at 1.6 m/s, showing smaller amplitudes of P300 and slightly smaller amplitudes of pre-stimulus than the raw signals in both scalp- and ear-EEG. The FFT-based method had the smallest amplitudes at all time intervals including P300 and pre-stimulus. The greater the signal distortion, the greater the effect of artifact removal, so that the SNRs at 2.0 m/s had great differences between the raw signals and all methods, particularly cIOL and rASR were higher than the raw signals. In Fig. 5b, the signed r^2 values, targets minus non-targets, can be related to the classification performance [49]. The cIOL had the largest signed r^2 values of N200 and P300 among all methods at all speeds in both scalp- and ear-EEG, particularly without much difference from even the raw signals at 2.0 m/s. In the view point of the AUC, the cIOL had the highest AUC among all methods and raw signals at all speeds in both scalp- and ear-EEG, particularly at 2.0 m/s.

B. SSVEP Performance

The SSVEP performance indicates how the artifact removal methods impact the frequency-dependent features in EEG signals. As shown in Fig. 7a, the ASR removed almost half the magnitude in low frequency range under 5 Hz, including the stepping frequency. Although the amplitude ratio of the ASR was much higher than that of the other methods (Fig. 7b), the BCI performance was impaired because of the moderate signal loss even at the target frequency (Fig. 8). In Fig. 7a, the rASR maintained a large amplitude over the entire frequency range compared to the other methods. The FFT-based method removed the entire frequency range, including the stepping frequency and target frequencies, particularly high frequency ranges. On the other hand, cIOL removed the components around the stepping frequency without deterioration at the target frequencies, except for 2.0 m/s. In the case of 2.0 m/s, there was a superposition problem between the harmonics of the target frequency and the harmonics of the stepping frequency, which showed low amplitudes at both the stepping frequency and the target frequency. Since the cIOL removed the artifacts, including the harmonics of stepping frequency, it had the low amplitude, particularly at 5.45 Hz (Fig. 7a), and the low SNR (Fig. 8b), but the much higher accuracy (Fig. 8a).

C. Reference Signals

Although several studies have used IMU as a reference to movement information, some have verified that IMU cannot accurately represent movement [23], [24]. Fig. 9 shows reference signals from IMU and isolated PC and signals after applying cICA with IMU and isolated PC in the time and frequency domains. Although the estimated artifacts were similar in both reference signals, the isolated PC tends to follow EEG signals that are closer to compatible representations of movement artifacts (Fig. 9). After applying IMU-based cIOL and isolated PC-based cIOL, the performances were similar, but slightly

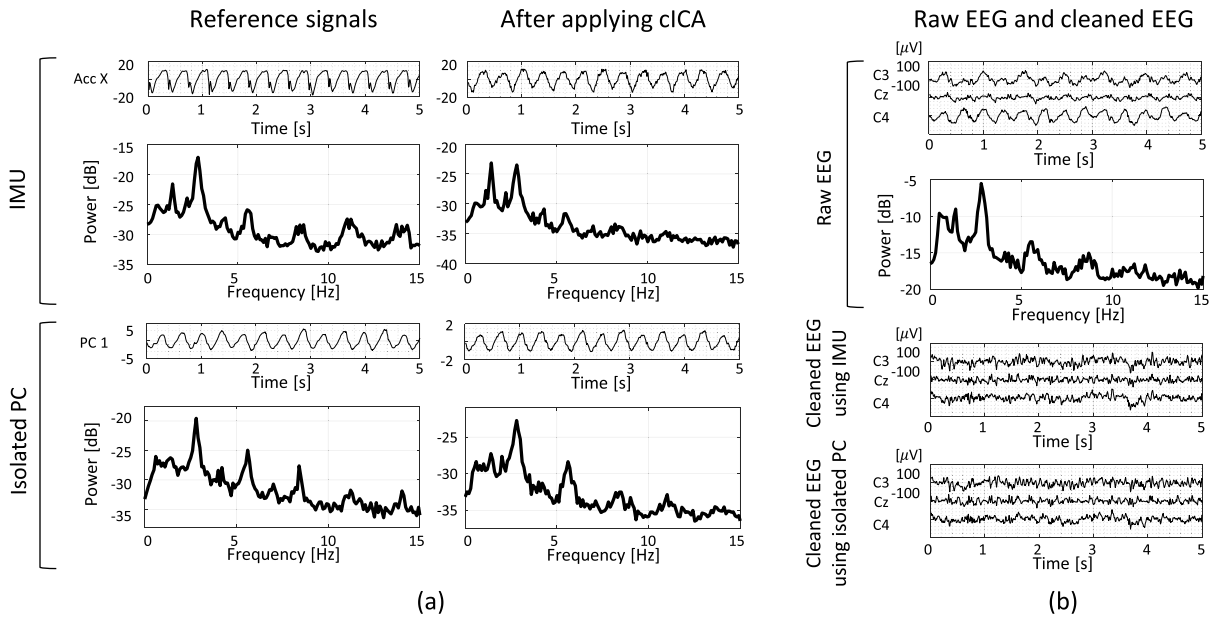

Fig. 9. Comparison of the reference signals from IMU sensors and isolated electrodes. (a) Example signals and the grand average of PSD in a light running session (2.0 m/s) of IMU sensor and isolated PC (left column) and their signals after applying cICA (right column). (b) Example signals and the grand average of PSD in a light running session (2.0 m/s) of raw EEG signals and the example of cleaned EEG signals using IMU-based cIOL and isolated PC-based cIOL.

higher in the isolated reference signals for the ERP and SSVEP in scalp- and ear-EEG. The performance of the IMU-based cIOL is shown in the supplementary documentation.

V. Conclusion

In this article, we proposed a real-time movement artifact removal method, cIOL, which is constrained ICA with online learning to remove artifacts and retain important components for recognizing human intentions. Isolated signals were obtained by blocking the brain signals using high-resistance materials. With the isolated signals, cICA estimated the movement artifacts from the EEG signals. And then online learning updated the weights in each sample and extracted artifact-free EEG signals. We collected data of scalp- and ear-EEG using two BCI paradigms, ERP and SSVEP, at four different speeds of 0, 0.8, 1.6, and 2.0 m/s. We evaluated movement artifact removal methods via the PSD and BCI performance from the viewpoint of the accuracy and SNR. In the evaluation, comparisons with the state-of-the-art methods, including ASR [18], rASR [14], and FFT-based method [13] were performed. The accuracy of cIOL showed that the highest among those of the signals in both scalp- and ear-EEG for both the ERP and SSVEP. In addition, the SNRs of cIOL in scalp-EEG for both the ERP and SSVEP showed the highest among those of applying the other methods, except for the SSVEP at 2.0 m/s. For the SSVEP at 2.0 m/s, the SNR of cIOL was lower than those of the other methods because of the superposition between stepping and target frequencies, but the accuracy of cIOL was higher than those of the other methods. Moreover, the isolated electrodes showed similar but little higher performance, compared to the reference signals using IMU sensors. In the future, we will extend the movement artifact removal method to all artifacts, not only movement ones. Moreover, we will improve the method to increase the SNR while maintaining the accuracy. Further, to increase the accuracy in an ambulatory environment, it is necessary to develop robust architectures that include verifying preprocessing parts, such as artifact detection [53], and developing a classification phase, as well. Therefore, we plan to build a total framework including the preprocessing phase with verification and the classification phase.

Acknowledgment

The authors would like to thank M. Lee and J.-H. Jeong for their help with advising the research, and G.-H. Shin for his assistance with data collection.

References

[1] J. Wolpaw, N. Birbaumer, D. McFarland, G. Pfurtscheller, and T. Vaughan, "Brain-computer interfaces for communication and control," *Clin. Neurophys.*, vol. 113, no. 6, pp. 767–791, Jun. 2002.

[2] K.-T. Kim, H.-I. Suk, and S.-W. Lee, "Commanding a brain-controlled wheelchair using steady-state somatosensory evoked potentials," *IEEE Trans. Neural Syst. Rehabil. Eng.*, vol. 26, no. 3, pp. 654–665, Mar. 2018.

[3] H.-I. Suk and S.-W. Lee, "A novel Bayesian framework for discriminative feature extraction in brain-computer interfaces," *IEEE Trans. Pattern Anal. Mach. Intell.*, vol. 35, no. 2, pp. 286–299, Feb. 2013.

[4] K. Gramann, J. T. Gwin, N. Bigdely-Shamlo, D. P. Ferris, and S. Makeig, "Visual evoked responses during standing and walking," *Frontiers Hum. Neurosci.*, vol. 4, p. 202, Oct. 2010.

[5] T. C. Bulea, J. Kim, D. L. Damiano, C. J. Stanley, and H.-S. Park, "Prefrontal, posterior parietal and sensorimotor network activity underlying speed control during walking," *Frontiers Hum. Neurosci.*, vol. 9, p. 247, May 2015.

[6] T. P. Luu, S. Nakagome, Y. He, and J. L. Contreras-Vidal, "Real-time EEG-based brain-computer interface to a virtual avatar enhances cortical involvement in human treadmill walking," *Sci. Rep.*, vol. 7, no. 1, p. 8895, Aug. 2017.

[7] B. R. Malcolm, J. J. Foxe, J. S. Butler, W. B. Mowrey, S. Molholm, and P. De Sanctis, "Long-term test-retest reliability of event-related potential (ERP) recordings during treadmill walking using the mobile brain/body imaging (MoBI) approach," *Brain Res.*, vol. 1716, pp. 62–69, Aug. 2019.

[8] E.-R. Symeonidou, A. Nordin, W. Hairston, and D. Ferris, "Effects of cable sway, electrode surface area, and electrode mass on electroencephalography signal quality during motion," *Sensors*, vol. 18, no. 4, Apr. 2018, Art. no. 1073.

[9] J. T. Gwin, K. Gramann, S. Makeig, and D. P. Ferris, "Removal of movement artifact from high-density EEG recorded during walking and running," *J. Neurophysiol.*, vol. 103, no. 6, pp. 3526–3534, Jun. 2010.

[10] T. Castermans *et al.*, "Optimizing the performances of a P300-based brain–computer interface in ambulatory conditions," *IEEE J. Emerg. Sel. Topics Circuits Syst.*, vol. 1, no. 4, pp. 566–577, Dec. 2011.

[11] J. Li *et al.*, "A unified canonical correlation analysis-based framework for removing gradient artifact in concurrent EEG/fMRI recording and motion artifact in walking recording from EEG signal," *Med. Biol. Eng. Comput.*, vol. 55, no. 9, pp. 1669–1681, Feb. 2017.

[12] E. Arad, R. P. Bartsch, J. W. Kantelhardt, and M. Plotnik, "Performance-based approach for movement artifact removal from electroencephalographic data recorded during locomotion," *PLoS ONE*, vol. 13, no. 5, May 2018, Art. no. e0197153.

[13] A. D. Nordin, W. D. Hairston, and D. P. Ferris, "Dual-electrode motion artifact cancellation for mobile electroencephalography," *J. Neural Eng.*, vol. 15, no. 5, Aug. 2018, Art. no. 056024.

[14] S. Blum, N. S. J. Jacobsen, M. G. Bleichner, and S. Debener, "A Riemannian modification of artifact subspace reconstruction for EEG artifact handling," *Frontiers Hum. Neurosci.*, vol. 13, p. 141, Apr. 2019.

[15] N.-S. Kwak, K.-R. Müller, and S.-W. Lee, "A lower limb exoskeleton control system based on steady state visual evoked potentials," *J. Neural Eng.*, vol. 12, no. 5, Aug. 2015, Art. no. 056009.

[16] Y.-E. Lee and M. Lee, "Decoding visual responses based on deep neural networks with ear-EEG signals," in *Proc. 8th Int. Winter Conf. Brain-Comput. Interface (BCI)*, Feb. 2020, pp. 1–6.

[17] N.-S. Kwak, K.-R. Müller, and S.-W. Lee, "A convolutional neural network for steady state visual evoked potential classification under ambulatory environment," *PLoS ONE*, vol. 12, no. 2, Feb. 2017, Art. no. e0172578.

[18] T. Mullen *et al.*, "Real-time modeling and 3D visualization of source dynamics and connectivity using wearable EEG," in *Proc. 35th Annu. Int. Conf. IEEE Eng. Med. Biol. Soc. (EMBC)*, Jul. 2013, pp. 2184–2187.

[19] T. R. Mullen *et al.*, "Real-time neuroimaging and cognitive monitoring using wearable dry EEG," *IEEE Trans. Biomed. Eng.*, vol. 62, no. 11, pp. 2553–2567, Nov. 2015.

[20] J. A. Palmer, S. Makeig, K. Kreutz-Delgado, and B. D. Rao, "Newton method for the ICA mixture model," in *Proc. IEEE Int. Conf. Acoust., Speech Signal Process.*, Mar. 2008, pp. 1805–1808.

[21] A. Kilicarslan, R. G. Grossman, and J. L. Contreras-Vidal, "A robust adaptive denoising framework for real-time artifact removal in scalp EEG measurements," *J. Neural Eng.*, vol. 13, no. 2, Feb. 2016, Art. no. 026013.

[22] A. Kilicarslan and J. L. Contreras Vidal, "Characterization and real-time removal of motion artifacts from EEG signals," *J. Neural Eng.*, vol. 16, no. 5, Sep. 2019, Art. no. 056027.

[23] J. E. Kline, H. J. Huang, K. L. Snyder, and D. P. Ferris, "Isolating gait-related movement artifacts in electroencephalography during human walking," *J. Neural Eng.*, vol. 12, no. 4, Jun. 2015, Art. no. 046022.

[24] K. L. Snyder, J. E. Kline, H. J. Huang, and D. P. Ferris, "Independent component analysis of gait-related movement artifact recorded using EEG electrodes during treadmill walking," *Frontiers Hum. Neurosci.*, vol. 9, p. 639, Dec. 2015.

[25] A. S. Oliveira, B. R. Schlink, W. D. Hairston, P. König, and D. P. Ferris, "Induction and separation of motion artifacts in EEG data using a mobile phantom head device," *J. Neural Eng.*, vol. 13, no. 3, May 2016, Art. no. 036014.

[26] A. D. Nordin, W. D. Hairston, and D. P. Ferris, "Human electrocortical dynamics while stepping over obstacles," *Sci. Rep.*, vol. 9, no. 1, p. 4693, Mar. 2019.

[27] A. S. Oliveira, B. R. Schlink, W. D. Hairston, P. König, and D. P. Ferris, "Proposing metrics for benchmarking novel EEG technologies towards real-world measurements," *Frontiers Hum. Neurosci.*, vol. 10, p. 188, May 2016.

[28] M.-H. Lee, J. Williamson, D.-O. Won, S. Fazli, and S.-W. Lee, "A high performance spelling system based on EEG-EOG signals with visual feedback," *IEEE Trans. Neural Syst. Rehabil. Eng.*, vol. 26, no. 7, pp. 1443–1459, Jul. 2018.

[29] D.-O. Won, H.-J. Hwang, D.-M. Kim, K.-R. Müller, and S.-W. Lee, "Motion-based rapid serial visual presentation for gaze-independent brain-computer interfaces," *IEEE Trans. Neural Syst. Rehabil. Eng.*, vol. 26, no. 2, pp. 334–343, Feb. 2018.

[30] Y.-P. Lin, Y. Wang, C.-S. Wei, and T.-P. Jung, "Assessing the quality of steady-state visual-evoked potentials for moving humans using a mobile electroencephalogram headset," *Frontiers Hum. Neurosci.*, vol. 8, p. 182, Mar. 2014.

[31] F. Popescu, S. Fazli, Y. Badower, B. Blankertz, and K.-R. Müller, "Single trial classification of motor imagination using 6 dry EEG electrodes," *PLoS ONE*, vol. 2, no. 7, Jul. 2007, Art. no. e637.

[32] Y. Chen *et al.*, "A high-security EEG-based login system with RSVP stimuli and dry electrodes," *IEEE Trans. Inf. Forensics Security*, vol. 11, no. 12, pp. 2635–2647, Dec. 2016.

[33] S. Debener, R. Emkes, M. De Vos, and M. Bleichner, "Unobtrusive ambulatory EEG using a smartphone and flexible printed electrodes around the ear," *Sci. Rep.*, vol. 5, no. 1, p. 16743, Nov. 2015.

[34] V. Goverdovsky, D. Looney, P. Kidmose, and D. P. Mandic, "In-ear EEG from viscoelastic generic earpieces: Robust and unobtrusive 24/7 monitoring," *IEEE Sensors J.*, vol. 16, no. 1, pp. 271–277, Jan. 2016.

[35] P. Kidmose, D. Looney, M. Ungstrup, M. L. Rank, and D. P. Mandic, "A study of evoked potentials from ear-EEG," *IEEE Trans. Biomed. Eng.*, vol. 60, no. 10, pp. 2824–2830, Oct. 2013.

[36] D. Looney *et al.*, "The in-the-ear recording concept: User-centered and wearable brain monitoring," *IEEE Pulse*, vol. 3, no. 6, pp. 32–42, Nov. 2012.

[37] M. G. Bleichner and S. Debener, "Concealed, unobtrusive ear-centered EEG acquisition: CEEGrids for transparent EEG," *Frontiers Hum. Neurosci.*, vol. 11, p. 163, Apr. 2017.

[38] N.-S. Kwak and S.-W. Lee, "Error correction regression framework for enhancing the decoding accuracies of ear-EEG brain–computer interfaces," *IEEE Trans. Cybern.*, vol. 50, no. 8, pp. 3654–3667, Aug. 2020.

[39] D.-O. Won, H.-J. Hwang, S. Dähne, K.-R. Müller, and S.-W. Lee, "Effect of higher frequency on the classification of steady-state visual evoked potentials," *J. Neural Eng.*, vol. 13, no. 1, Dec. 2015, Art. no. 016014.

[40] M.-H. Lee *et al.*, "EEG dataset and OpenBMI toolbox for three BCI paradigms: An investigation into BCI illiteracy," *GigaScience*, vol. 8, no. 5, Jan. 2019, Art. no. giz002.

[41] R. Krepki, B. Blankertz, G. Curio, and K.-R. Müller, "The berlin brain-computer interface (BBCI)—Towards a new communication channel for online control in gaming applications," *Multimedia Tools Appl.*, vol. 33, no. 1, pp. 73–90, Feb. 2007.

[42] C. A. Kothe and S. Makeig, "BCILAB: A platform for brain–computer interface development," *J. Neural Eng.*, vol. 10, no. 5, Aug. 2013, Art. no. 056014.

[43] M. Kleiner, D. Brainard, and D. Pelli, "What's new in Psychtoolbox-3?" *Perception ECVP Abstr. Suppl.*, vol. 36, p. 14, Jan. 2007.

[44] S. Raychaudhuri, J. M. Stuart, and R. B. Altman, "Principal components analysis to summarize microarray experiments: Application to sporulation time series," in *Proc. Biocomputing*, Dec. 1999, pp. 455–466.

[45] W. Lu and J. C. Rajapakse, "Constrained independent component analysis," in *Proc. Adv. Neural. Inf. Process. Syst.*, May 2001, pp. 570–576.

[46] C. J. James and O. J. Gibson, "Temporally constrained ICA: An application to artifact rejection in electromagnetic brain signal analysis," *IEEE Trans. Biomed. Eng.*, vol. 50, no. 9, pp. 1108–1116, Sep. 2003.

[47] H. H. Yang and S.-I. Amari, "Adaptive online learning algorithms for blind separation: Maximum entropy and minimum mutual information," *Neural Comput.*, vol. 9, no. 7, pp. 1457–1482, Oct. 1997.

[48] S. S. Haykin, *Adaptive Filter Theory*. Noida, India: Pearson Education, 2005.

[49] B. Blankertz, S. Lemm, M. Treder, S. Haufe, and K.-R. Müller, "Single-trial analysis and classification of ERP components—A tutorial," *NeuroImage*, vol. 56, no. 2, pp. 814–825, May 2011.

[50] M. De Vos, K. Gandras, and S. Debener, "Towards a truly mobile auditory brain–computer interface: Exploring the P300 to take away," *Int. J. Psychophysiol.*, vol. 91, no. 1, pp. 46–53, Jan. 2014.

[51] M. Nakanishi, Y. Wang, Y.-T. Wang, Y. Mitsukura, and T.-P. Jung, "Generating visual flickers for eliciting robust steady-state visual evoked potentials at flexible frequencies using monitor refresh rate," *PLoS ONE*, vol. 9, no. 6, Jun. 2014, Art. no. e99235.

[52] H. Schimmel, "The (±) reference: Accuracy of estimated mean components in average response studies," *Science*, vol. 157, no. 3784, pp. 92–94, Jul. 1967.

[53] Q. Barthelemy, L. Mayaud, D. Ojeda, and M. Congedo, "The Riemannian potato field: A tool for online signal quality index of EEG," *IEEE Trans. Neural Syst. Rehabil. Eng.*, vol. 27, no. 2, pp. 244–255, Feb. 2019.